A Creep Model with Different Properties Under Tension and Compression – Applications to Refractory Materials

Lucas Teixeira, Jean Gillibert, Thomas Sayet, Eric Blond

Univ. Orléans, Univ. Tours, INSA-CVL, LaMé
8 Rue Léonard de Vinci, 45072, Orléans, France

Abstract

Refractories are materials designed to work at high temperatures, and are applied in steel making, cement making, aerospace engineering, and other fields where a combination of chemical and mechanical stability is paramount. Due to such high temperature applications, creep strains play an important role in the mechanical performance of refractories, that often present an asymmetric behavior, i.e., different creep strain rates under tension and compression. The aim of this work is to propose an asymmetric creep model that can be used to simulate the time-dependent non-linear primary and secondary creep behavior of refractories at high temperature. The proposed model uses a split of the stress tensor into positive and negative parts and further calculation of the contribution of each stress sign to the overall strain rate using a weighted average over the equivalent stresses. An experimental procedure is proposed in order to identify the tensile and compressive parameters of an alumina-spinel refractory used in steel ladle linings, using a Brazilian test and a subset-based Digital Image Correlation (DIC) technique, for a temperature of 1300 °C.

Keywords: Asymmetric Creep, Refractories, Finite Elements, Modeling

List of Symbols

$\underline{\underline{\sigma}}$	Second rank stress tensor
σ_{eq}	Von Mises equivalent stress
σ_x	Stress in direction x
σ_y	Stress in direction y
f_y	Yield stress
$\underline{\underline{s}}$	Second rank deviatoric stress tensor
σ_t	Tensile strength
σ_c	Compression strength
ε_x	Total strain in direction x
ε_y	Total strain in direction y
p	Equiv. creep (viscoplastic) strain
$\underline{\underline{\dot{\varepsilon}}}^{cr}$	Second rank creep (viscoplastic) strain rate tensor
E	Young's modulus
ν	Poisson's ratio
A, n, m	Temperature dependent creep parameters
w	Weights
e	Sample's thickness
ϕ_s	Sample's diameter
ϕ_j	Jaws' diameter
$\underline{\underline{I}}$	Identity matrix
$Tr()$	Trace
$\langle \quad \rangle$	Macaulay brackets
$x^{\pm}$	Positive and negative parts of variable x
F	Force
t	Time

1. Introduction

Refractories are materials designed to work at highly aggressive environments, and need to resist to thermo-mechanical stresses and strains, corrosion and erosion at temperatures that can reach over 2000 °C (Banerjee, 2004). In the production of steel, cement, glass, copper, between other materials processed at high temperatures, the goal of refractory linings is to protect the vessels used in the production process, normally made of steel, from overheating and consequent mechanical failure, as well as to control the heat losses from the process (Schacht, 2004).

The transformation of raw materials into finished steel products involve high temperature processes, and different vessels lined with refractories are used to contain the molten metals, such as blast furnaces, basic oxygen furnaces (BOFs), electric arc furnaces (EAFs), ladles and tundishes. Among those vessels, the steel ladle has a considerable importance, since it is used in the secondary metallurgy, where a considerable amount of time and financial resources have already been previously employed on the production process, and is responsible for a non-negligible consumption of refractories (Dutta & Chokshi, 2020). The integrity of the ladle is of central importance to the safety of the production site, since it transits between other equipments and workers, carrying molten steel, and a failure can lead to serious consequences.

Figure 1a shows a cutaway view of a steel ladle, and Figure 1b shows a schematic representation of the top view of one ring of a ladle lining. The choice of the refractories to be applied in each layer of the lining greatly influences the temperature distribution in the ladle, therefore playing also a crucial role on its thermo-mechanical behavior (Volkova & Janke, 2005) and on the energy consumption.

An important phenomena to be considered in the design of the steel ladle is the creep and stress relaxation of the refractory lining. The absence of a non-linear viscoplastic behavior can lead to stress values that can't be supported by the vessel, causing a mechanical failure. Nevertheless, if the material presents

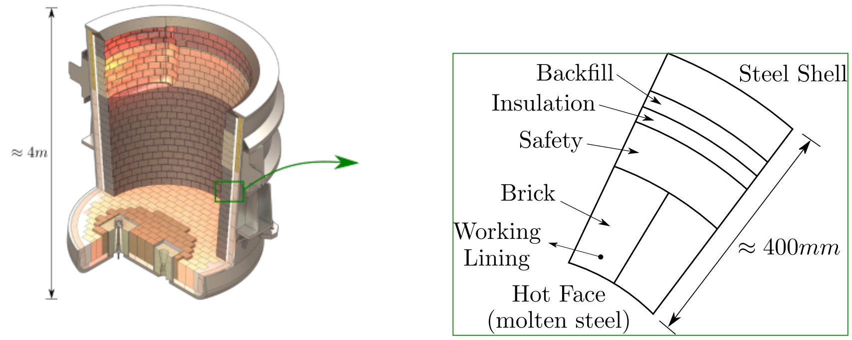

(a) (b)

Figure 1: Example of a steel ladle. (a) Cutaway view showing the refractory linings. (b) Schematic representation of a line ring, top view.

excessive creep, it will have a considerable reduction on its size caused by the compression stresses at the hot face. During the cooling of the ladle, joints may open, making the lining loose and allowing for steel infiltration in posterior production cycles. Therefore, the design of the refractory lining and of the steel shell can benefit from a numerical model that can predict more accurately the stress and strain variations over time, and the effect of thermal cycles can be taken into account to maximize the vessel's life.

Due to the complexity of their mechanical behavior, the modeling and simulation of refractory materials has often been restricted to the application of simple constitutive models, in some cases even neglecting the well known non-linearity of the material (Jin et al., 2011). In other cases, creep models have been applied to simulate the thermo-mechanics of refractories, but considering a symmetric behavior and using the compressive mechanical properties (Jin et al., 2020). There were also attempts to use a Drucker-Prager-based creep model to simulate the effect of the material's asymmetry of RH-degassers lining behavior, but the authors concluded that this model might not be ideal and that more complex representation of the actual behavior should probably be used (Jin et al., 2015).

In this work, an asymmetric creep model is proposed, which is able to represent the different behavior that refractory materials present under tension and compression. The main goal is to obtain a relatively simple constitutive model, that can have the material parameters identified using the least possible number of mechanical tests, due to the need to characterize the material at several temperatures, which requires a high time and energy consumption. With the proposed model, the lifetime of refractory materials can be predicted more accurately than the using current engineering practice (linear elastic or symmetric creep models), since it accounts for the significant increase in the creep strain rate when tensile loads are present in the lining. Similarly, the model allows for a better comparison between the performance of products with different shapes and compositions, reducing field trials and improving the availability of the equipments.

Section 2 provides a description of the current creep models available in the literature, explaining what are the missing features when the simulation of refractory materials need to be done. Section 3 describes the proposed model, and comments on possible numerical difficulties that can arise when implementing it, as well as numerical strategies that can be used to mitigate them. Section 4 presents numerical simulations used to theoretically validate the proposed model. Section 5 describes the high temperature experimental procedure used to characterize the material, with a detailed explanation of the reason why the Brazilian test method was used. Finally, Section 6 presents the identification of the material parameters of an alumina-spinel brick used in steel ladles.

2. Symmetric and asymmetric creep models

The creep behavior of ceramic materials can be split in three stages. The first stage, called primary creep, presents a time-dependent strain rate which decreases with time. In the secondary creep stage, the strain rate is considered to be constant, and an approximate equilibrium between hardening and softening processes can be assumed (Naumenko & Altenbach, 2007). Finally, in the third creep stage, the strain rate increases with time until the failure of the material

(Jin et al., 2014).

2.1. Symmetric creep models

One of the most traditional creep models available in the literature is based on the one-dimension Norton-Bailey's law, known on its multi-dimensional version as Odqvist's law (Lemaître & Chaboche, 1990), which relates the creep strain rate $\dot{\underline{\underline{\varepsilon}}}^{cr}$ to the stresses using the following equation:

$$\dot{\underline{\underline{\varepsilon}}}^{cr} = \frac{3}{2}\underline{\underline{s}}A\sigma_{eq}^{n-1}p^{m} \tag{1}$$

where $\underline{\underline{s}}$ is the deviatoric component of the stress tensor, σ_{eq} is the von Mises equivalent stress, p is the equivalent viscoplastic strain (sometimes refered to as equivalent creep strain) and A, n, and m are temperature dependent material parameters. For the case of secondary creep, $m = 0$. The Norton-Bailey's law have been extensively used to characterize refractory materials, due to its simplicity and good fitness to experimental results (Jin et al., 2014; Samadi et al., 2020; Schachner et al., 2019; Sidi Mammar et al., 2016; Teixeira et al., 2020).

If an elastic region needs to be considered in the model, a simple modification in Equation 1 can be done to take it into consideration (Lemaître & Chaboche, 1990):

$$\dot{\underline{\underline{\varepsilon}}}^{cr} = \frac{3}{2}\frac{\underline{\underline{s}}}{\sigma_{eq}}A\left\langle \sigma_{eq} - f_y \right\rangle^{n} p^{m} \tag{2}$$

where f_y is the yield stress and $\langle \quad \rangle$ are the Macaulay brackets.

It should be noted that different uniaxial laws other than Norton-Bailey's law can be applied to relate the stresses to the creep strains (Lemaître & Chaboche, 1990). The choice of which law should be used depends on how accurately it fits the mechanical tests.

2.2. Asymmetric creep models

As can be noticed in Equations 1 and 2, the Norton-Bailey creep model is not able to represent materials with different behaviors under tension and compression (asymmetric creep).

The asymmetry in the material's response was approached by Altenbach (2001) using a creep strain rate formulation that depends on three linear independent invariants of the stress tensor. Alternatively, Mahnken (2003) proposed an asymmetric creep model that uses a scalar variable expressed in terms of the ratio of the second and third invariants of the deviatoric stress tensor, called stress mode angle in the octahedral plane in the deviatoric stress space.

Although these models are mathematically consistent and were successfully applied, they present the inconvenient to require a considerable number of experiments to determine the creep parameters, since tension and compression behaviors are not decoupled. For the case of refractories, that need to be characterized at several temperatures, this represents a limitation.

More recently, Samadi et al. (2021) coupled the asymmetric primary creep behavior of refractories with a damage model. In this model, the equation for the creep strain rate is selected according to the sign of the principal stresses, without any particular weighting strategy, and the equations are solved using an explicit integration scheme.

To account for the asymmetric creep of refractories, Blond et al. (2005) extended the Norton-Bailey's model, using a split of the principal stress vectors into a positive and a negative parts, to propose a secondary creep model, resulting in:

$$\underline{\underline{\sigma}} = \left\langle \underline{\underline{\sigma}} \right\rangle - \left\langle -\underline{\underline{\sigma}} \right\rangle \tag{3}$$

This split results in the definition of the model in terms of independent tension and compression parameters. In this sense, the two parts of the deviatoric stress tensor are given by:

$$\underline{\underline{s}}^{\pm} = \left\langle \pm\underline{\underline{\sigma}} \right\rangle - \frac{1}{3} Tr(\left\langle \pm\underline{\underline{\sigma}} \right\rangle)\underline{\underline{I}} \tag{4}$$

where the indexes $\pm$ indicate the positive and negative parts of the variables,

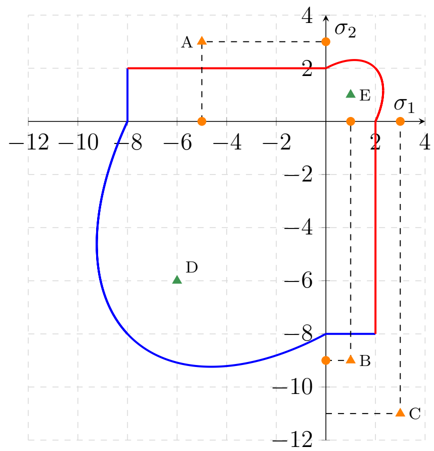

Figure 2: Yield surface of Blond's model.

respectively. The equivalent von Mises stresses are, then:

$$\sigma_{eq}^{\pm} = \sqrt{\frac{3}{2}\underline{\underline{s}}^{\pm} : \underline{\underline{s}}^{\pm}} \tag{5}$$

resulting in a viscoplastic strain rate of the form:

$$\dot{\underline{\underline{\varepsilon}}}_{cr} = \frac{3}{2}\frac{\underline{\underline{s}}^{+}}{\sigma_{eq}} A^{+} \left\langle \sigma_{eq}^{+} - f_y^{+} \right\rangle^{n^{+}} - \frac{3}{2}\frac{\underline{\underline{s}}^{-}}{\sigma_{eq}} A^{-} \left\langle \sigma_{eq}^{-} - f_y^{-} \right\rangle^{n^{-}} \tag{6}$$

where $A^{\pm}$ and $n^{\pm}$ are material's constants in tension (+) and compression (−).

Figure 2 shows a representation of Blond's model in the 2D principal stresses domain. In this example, the tensile yield stress is $f_y^{+} = 2$ MPa and the compressive yield stress is $f_y^{-} = -8$ MPa. In the figure, the stress states D and E marked as green triangles are inside the elastic region, therefore no creep is observed.

Point A shows a stress state in the second quadrant, with a compressive component in direction 1 and a tensile component in direction 2. Therefore, the stress split described by Equation 3 results in other two stress states, shown as circular markers. As can be seen, the point (-5, 0) is in the elastic region, so no creep is expected for the compressive component. On the other hand, the point (0, 3) lays outside the elastic region, so the first term of the right hand side of

Equation 6 is activated, and creep in tension is observed.

Point B corresponds to the opposite situation, i.e., creep is activated in compression but not in tension. The stress state represented by Point C results in creep in both tension and compression.

From Figure 2, it is also evident that Blond's yield surface presents singularities at the points where it crosses axis 1 and 2, as well as in the corners present in the second and fourth quadrants. When the structure being modeled has stress states close to these singularities, difficulty in the convergence may arise. Nevertheless, this should not be a problem if the yield stress is equal to zero, i.e., the material starts to creep as soon as a load of any magnitude is imposed, which is often the case for refractories (Jin et al., 2014).

One of the main advantages of this model is that the material's parameters for tensile and compression creep are completely independent, therefore they can be identified separately. This gives flexibility to fit the creep flow calculations to a large range of strain rates observed in experiments.

Nevertheless, the validity of the stress split hypothesis needs to be verified, and this model presents the characteristic of making a sum between two terms (positive and negative strain rates) that depend on the equivalent stress. The consequence of this fact is that, if this model is used with identical properties in tension and in compression, the resulting viscoplastic strain rate is not the same as the one obtained with a symmetric model. Although this is not necessarily a limitation, in some cases it can be desirable to have a model that is an interpolation of the tension and the compression material behaviors, without this intrinsic orthotropy.

As remarked by Esposito and Bonora (2011), in many applications the primary creep of materials can't be neglected, since a considerable part of the allowable design strain occurs in this stage. This is the case of the alumina-spinel material studied in this work, as it is evident by the creep curves previously published by Samadi et al. (2020) and Teixeira et al. (2020).

3. Proposition of an asymmetric creep model considering primary and secondary creep stages

3.1. Model description

In this work, to represent the primary and secondary creep behaviors of refractory materials, Equation 1 was adapted following the same principle of the split of the stress tensor in a positive and a negative part, as used by Blond et al. (2005).

The proposed model also differentiates from Blond's model in the way to consider the different contributions of the compression and tensile characteristics of the material. After the decomposition of the stress tensor, the deviatoric and equivalent stresses are calculated for each part (positive and negative) using Equations 4 and 5, respectively, such as in the model proposed by Blond et al. (2005).

Nevertheless, instead of using $\underline{\underline{s}}^{\pm}$ and $\sigma_{eq}^{\pm}$ to directly calculate the positive and negative viscoplastic strain rates (Equation 6), these values are used to calculate relative weights that each part of the stress tensor have on the total equivalent stress, using the relation:

$$w^{\pm} = \frac{\sigma_{eq}^{\pm}}{\sigma_{eq}} \tag{7}$$

Each portion of the viscoplastic strain rate is calculated as a function of the total deviatoric and equivalent stresses (using the full stress tensor, before the decomposition into positive and negative parts) and the respective material properties:

$$\dot{\underline{\underline{\varepsilon}}}^{cr^{\pm}} = f(\underline{\underline{s}}, \sigma_{eq}, A^{\pm}, n^{\pm}, m^{\pm}) \tag{8}$$

Later, each part of the viscoplastic strain rate is weighted by the values calculated using Equation 7. Therefore, the viscoplastic strain rate of the proposed asymmetric creep model is given by:

$$\dot{\underline{\underline{\varepsilon}}}^{cr} = w^{+} \cdot \frac{3}{2}\frac{\underline{\underline{s}}}{\sigma_{eq}} A^{+} \left\langle \sigma_{eq} - f_y^{+} \right\rangle^{n^{+}} p^{m^{+}} - w^{-} \cdot \frac{3}{2}\frac{\underline{\underline{s}}}{\sigma_{eq}} A^{-} \left\langle \sigma_{eq} - f_y^{-} \right\rangle^{n^{-}} p^{m^{-}} \tag{9}$$

This model is also similar to the one developed by Mahnken (2003), in the sense that it proposes a weighted calculation of the creep strain rate. Nevertheless, the model proposed here can be considered to be more straightforward, and it also requires less parameters to characterize the creep behavior of a given material, which is an important advantage. This model was implemented in an Abaqus UMAT subroutine, and examples of calculations are shown in the next sections. The integration algorithm according to Benallal et al. (1988) was used in this subroutine.

It should be noted that, when the material presents primary creep under compression and secondary creep under tension, such as in the case of the alumina-spinel brick, $m^- = 0$ in Equation 9. To summarize, Figure 3 presents flow charts corresponding to the algorithm proposed by Blond et al. (2005) (full lines) and the algorithm proposed in this work (dashed lines).

3.2. Numerical difficulties associated with primary creep

At the beginning of a structural simulation, when the load was not yet applied, the strain in the simulated body is assumed to be zero, unless otherwise stated. In this situation, it is reasonable to assume that the equivalent creep strain is $p = 0$. Examining Equation 9 and taking into account that the variable m can only take negative values, it is easy to deduce that:

$$\lim_{p \to 0} \dot{\underline{\underline{\varepsilon}}}^{cr} = 0 \tag{10}$$

Therefore, the equivalent viscoplastic strain can't be defined as zero at time $t = 0$, since this would result in the absence of creep strain in the subsequent time step, independently of the applied load.

The first solution to this problem is to define a low non-zero initial value for p. Nevertheless, it is not always clear which value should be used, since the convergence of the simulation is highly dependent on it. For example, consider a case where only compression creep is applied and $f_y = 0$. Equation 9 becomes:

$$\dot{\underline{\underline{\varepsilon}}}^{cr} = \frac{3}{2} \underline{\underline{s}} A^- \sigma_{eq}^{(n^- -1)} p^{m^-} \tag{11}$$

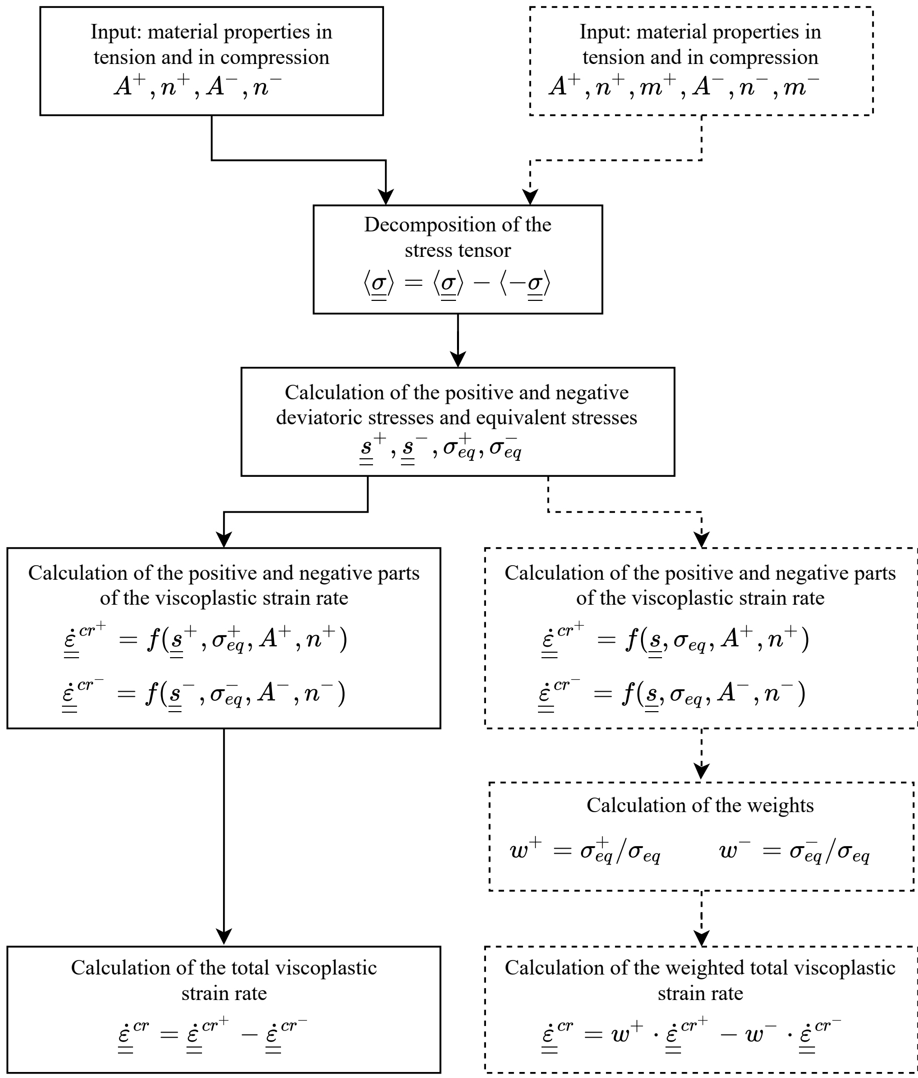

Figure 3: Asymmetric creep model algorithms. Blond et al. (2005) (full lines) and the proposition of this work(dashed lines)

Supposing $\underline{\underline{s}}$ and σ_{eq} to have an order of magnitude of 10, $A \approx 1 \times 10^{-10}$, $m \approx -2$, $n \approx 2$ and an initial approximation of $p = 1 \times 10^{-15}$, the resulting creep strain rate would be $\dot{\underline{\underline{\varepsilon}}}^{cr} \approx 1 \times 10^{22}$. A high value of initial creep strain rate is expected from primary creep, but at this rate of strain, the integration algorithm would have to use an extremely low time step value in order to converge, which is not practical.

It can be concluded that an initial equivalent viscoplastic strain value should be used so that it is small enough to do not decrease the accuracy of the solution and large enough to allow the convergence in a reasonable time frame. This value depends on the material properties, the applied loads, the boundary conditions and on the time stepping used during the solution, and can be considerably difficult to estimate.

To improve the convergence of the model, the following actions can be taken:

1. Given the material properties and boundary conditions of the problem, an initial value for the equivalent creep strain $p_{t=0}$ needs to be determined. The convergence of the initial steps of the model is tested, using a small time increment. If necessary, $p_{t=0}$ should be increased.
2. The time step increment should be small during the first seconds of loading, since the primary creep curve can be steep at the beginning. It can be interesting to brake the initial steps into smaller ones, to allow a finer control of the time increment.
3. Even when the initial moments of primary creep are past, the maximum increment of time should be limited to reasonable values, since the automatic time stepping control present in some FEA software can attempt to increase it beyond the convergence limit of the integration algorithm. Even if the software is able to converge, it can take many iterations to finish a step, leading to slower computations.

Even if those measures are taken, the simulation can still diverge due to a rapid change in the creep strain rate, specially for the case where tensile loads are meaningful. To limit this problem, in the UMAT subroutine used to implement the creep models developed in this work, a variable was implemented to control the convergence of the integration algorithm. If the algorithm does not converge, the subroutine automatically returns to the previous converged iteration, and tries a time step that is half the previous attempt. This action is only effective if the convergence problem is related to the integration algorithm of the constitutive equations, not to the global Newton-Raphson integration scheme.

4. Numerical simulations using the proposed asymmetric creep model

To evaluate the capabilities of the proposed asymmetric model, a set of numerical simulations is presented, in increasing order of complexity. The goal of these simulations is to verify if the model presents the expected behavior when subjected to complex load cases. The material parameters used to perform these tests are shown in Table 1. As it will become evident in the next sections, these material parameters are close to the one corresponding to the alumina-spinel material. It was considered that the tensile behavior of the material could be approximated by a secondary creep model, as discussed by Teixeira et al. (2020).

Table 1: Material parameters used in the numerical simulation tests

Parameter	**Compression**	**Tension**
$E[\mathrm{MPa}]$	30000	30000
$\nu[-]$	0.2	0.2
$\log_{10} A[\mathrm{MPa}^{-n}s^{-1}]$	-14.16	-5.4
$n[-]$	3.96	1.5
$m[-]$	-2.74	$-$

In the simulations, four situations regarding the type of model and the material parameters were considered:

1. Abaqus symmetric creep model using the compression properties of the material. This configuration is commonly seen in publications related to the creep of refractories, as previously cited.

2. Abaqus symmetric creep model using the tension properties of the material, used as a reference to compare with the asymmetric model.
3. UMAT asymmetric creep model, but using the compression properties of the material for compression and tension, to verify if the asymmetric model specializes to a symmetric one when necessary.
4. UMAT asymmetric creep model, using the corresponding properties for tension and compression.

4.1. Normal loads with stress reversal in two dimensions

The first model corresponds to a simple two-dimensional element (Figure 4a, where e is the thickness) subjected to a load path that varies in directions x and y, according to Figure 4b. The maximum tensile stress is $\sigma_t = 0.2$ MPa, and the minimum compression stress is $\sigma_c = -2.0$ MPa. Figures 4c and 4d show the time periods for which the stresses are kept in the sample.

Although this is a simple model, it represents a situation where, during the loading cycle, there are moments where both principal stresses are positive (Point B), both are negative (Point D), and when there is a composition of positive and negative stresses at the same integration point (Points C and E). Therefore, the simulation is useful to show the difference between a symmetric and an asymmetric model, as well as the effect of the loading history. For this model, an extra curve using the tension material parameters for both tension and compression material laws is also presented.

Figure 5 shows the accumulated viscoplastic strains computed in each of the situation previously described. It is possible to observe that, when the same properties are used for tension and compression, the UMAT provides the same results as a symmetric model. More importantly, the asymmetric model presents an intermediate response between the tension and the compression symmetric models, as expected.

In Figure 5 it is clear that, until approximately 30 min, when only tension stresses are present in the element (Points A and B in Figure 4), the symmetric and asymmetric models give the same result. From that point further, when

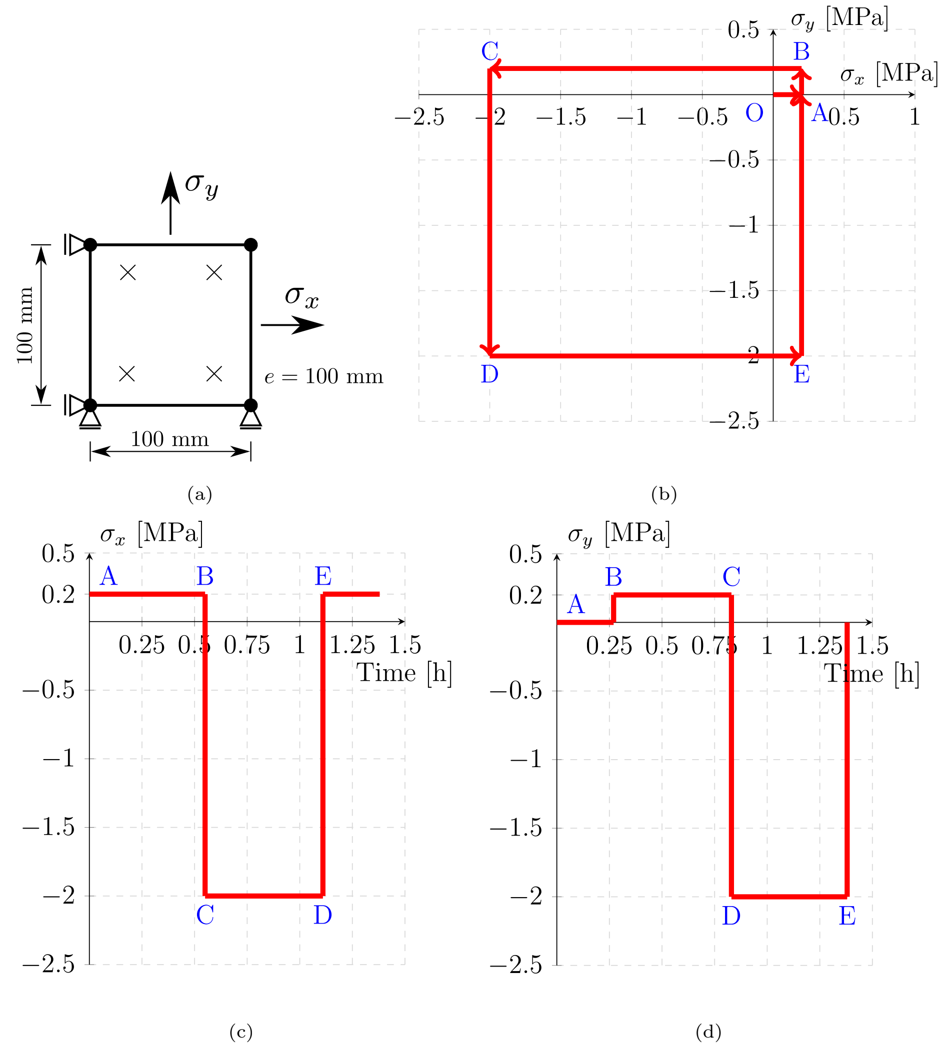

Figure 4: Stress distribution − Normal loads. (a) Simulation model. (b) Stress path. (c) σ_x vs Time. (d) σ_y vs Time.

an asymmetry is included in the loading (Point C in Figure 4), the model response changes, becoming an interpolation between the tension and compression behaviors.

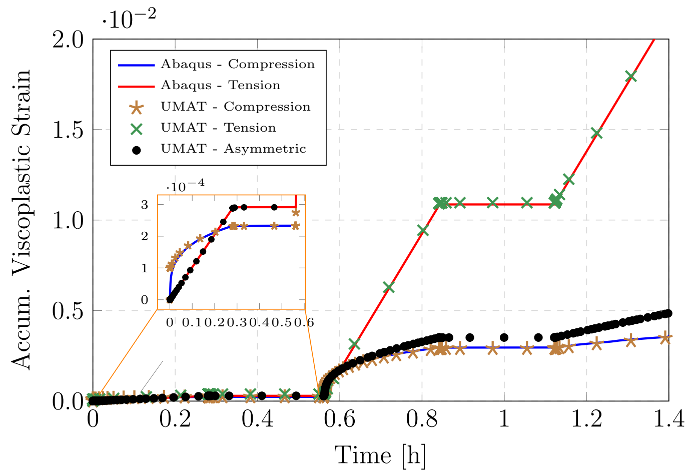

Figure 5: Accumulated viscoplastic strain − Normal loads.

4.2. Brazilian test

Figure 6 shows the geometry, mesh and boundary conditions used to compare the symmetric and asymmetric models applied to a Brazilian test specimen. The sample was discretized using linear square elements with full integration, unless for a transition zone between the refined mesh in the contact region and the rest of the geometry, where linear triangular elements with full integration were used.

The sample was modeled with $\phi_s = 50$ mm diameter and $e = 40$ mm thickness. Analytic rigid surfaces representing the upper and lower jaws with diameters $\phi_j = 65$ mm were used to distribute the load more evenly on the sample and to avoid excessive stress concentrations. The same strategy was used at the bottom part of the model to restrict the vertical displacement of the sample. Due to the geometry and force symmetries, only half of the sample was modeled.

A force of -400 N was applied on the model following a 30 s linear ramp, and it was kept for two hours. This geometry and boundary conditions are the same used for the mechanical tests at 1300 °C, presented in Section 5.

A comparison between vertical and horizontal displacements taken at the center of the sample for the four cases is shown in Figure 7. It is possible to

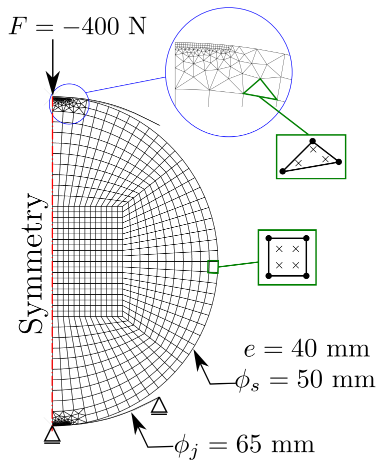

Figure 6: Brazilian test − Geometry, mesh and boundary conditions.

observe that, when compression curves are used in the asymmetric model, the result is in high agreement with the symmetric model available on the software Abaqus.

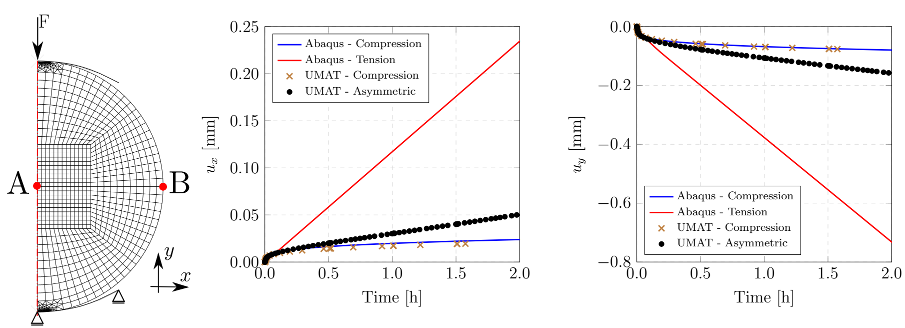

(a) (b)

Figure 7: (a) Vertical and (b) horizontal displacements in the Brazilian test sample.

Figures 8 and 9 show the maximum principal stress and the minimum principal stress on the sample, respectively, for the cases where only tension or compression material parameters were considered (symmetric creep), and the asymmetric case. It can be observed that the maximum tensile stress value obtained on the sample was 0.35 MPa. Since refractory materials are less resistant to tension, this stress limits the amount of force that can be applied before the failure of the sample. The maximum compressive stresses observed on the sample are in the range of -2.5 MPa to -3.8 MPa, although at the center of the sample this value does not go higher than -1.8 MPa. This can be considered as a limitation of the Brazilian test when compared to uniaxial tests for the identification of material parameters, i.e., the tension and compression loads are not decoupled, therefore the material can only be safely characterized for a smaller stress range. Nevertheless, this only represents a problem if, during operation, the actual compression stresses withstand by the material are considerably higher than the ones during the mechanical tests.

It should be noted that, in Figures 8 and 9, the contact zones were excluded from the results plots. This was done because, in these regions, the model can experiment stress concentrations, that makes the visualization of the plots more difficult in the other regions of the model. In a real experiment, these regions suffer from a local failure, with the crash of the grains at the contact with the jaws. This failure can normally be neglected in the experiment, but it can influence the convergence of the numerical model. For instance, the elements with higher stresses present, as a consequence, higher creep strain rate, and the model takes longer to converge due to the need of low time steps, even if the bulk part of the sample is still under low stresses. To use the proposed asymmetric model, attention should be payed to such stresses concentration areas, and they should be removed from the model, if possible.

When compared to a symmetric model using the compression creep properties, the asymmetric model has a considerably different behavior over time regarding the strains. Figure 10 shows that, over the central line of the sample, the total strain ε_x, that is mainly positive, is the same for both models at the end of loading (30 s). Nevertheless, after one hour, the strain obtained by the asymmetric model is approximately the double of the one obtained by the symmetric model, and after two hours the ratio between them is around three. The same proportional difference is observed on Figure 11 for the total strain ε_y, that is compressive. This fact is due to the averaged sum of the tension

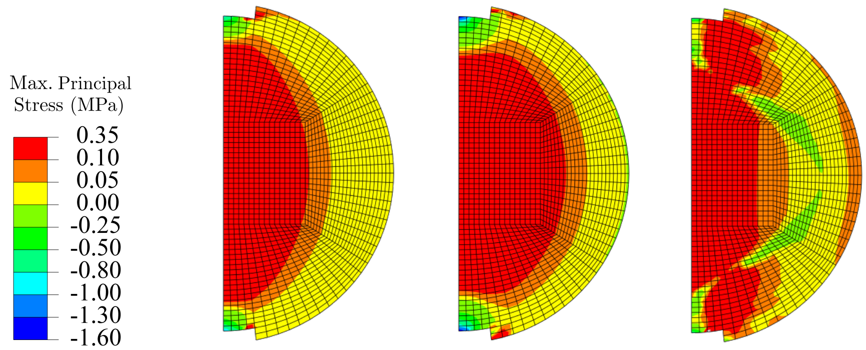

(a) (b) (c)

Figure 8: Maximum principal stress distribution on a Brazilian test sample. (a) compression (b) tension and (c) asymmetric material properties.

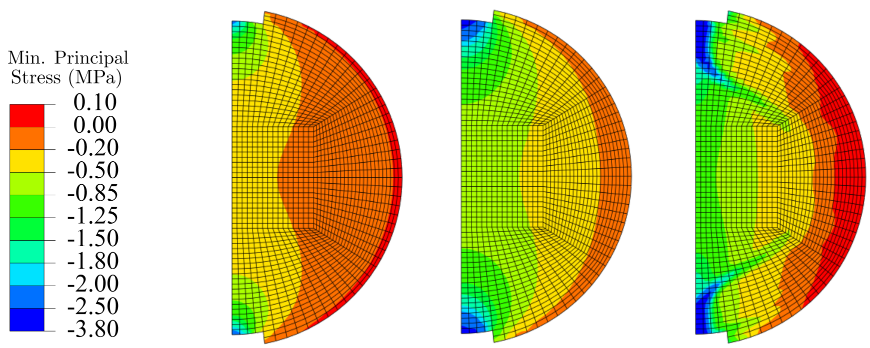

(a) (b) (c)

Figure 9: Minimum principal stress distribution on a Brazilian test sample. (a) compression (b) tension and (c) asymmetric material properties.

and compression creep strain rates applied by the asymmetric model, where the tension part contributes to considerably increase the value of the strains.

Finally, Figure 12 shows the effect of the asymmetry in the accumulated viscoplastic strain on a Brazilian test. Once again, the proposed asymmetric model shows an intermediary behavior between the symmetric ones, and evidences the importance of the consideration of the different material properties in tension and in compression.

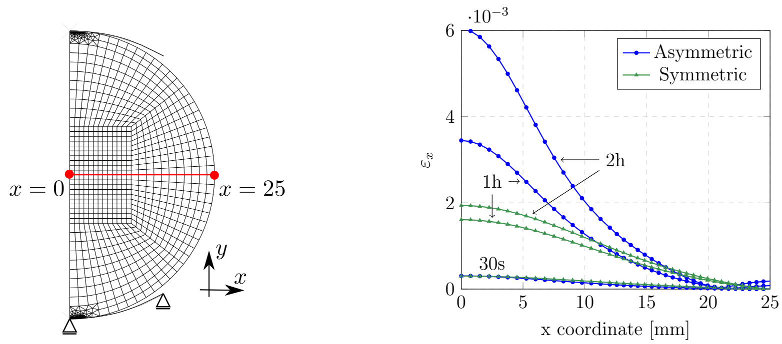

Figure 10: Variation of the total strain in direction x with time − Symmetric and asymmetric models.

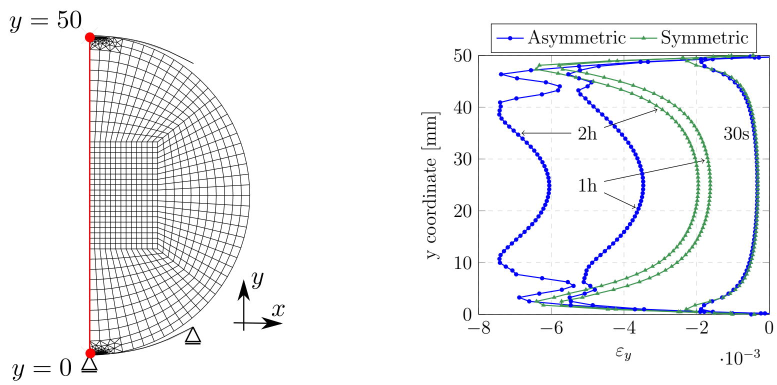

Figure 11: Variation of the total strain in direction y with time − Symmetric and asymmetric models.

4.2.1. Influence of the constitutive model parameters

To have a better idea on how each of the constitutive model parameters influences the results obtained from a Brazilian test simulation, calculations were made varying one parameter at a time around the absolute values of the nominal properties presented on Table 1 by −10%, −20%, +10% and +20%. These values are shown in Table 2. This method is not considered an accurate sensitivity analysis, and the intention is to qualitatively understand how the parameters influence the shape of the time-displacement curves, which is an useful information when an inverse identification of the parameters using real

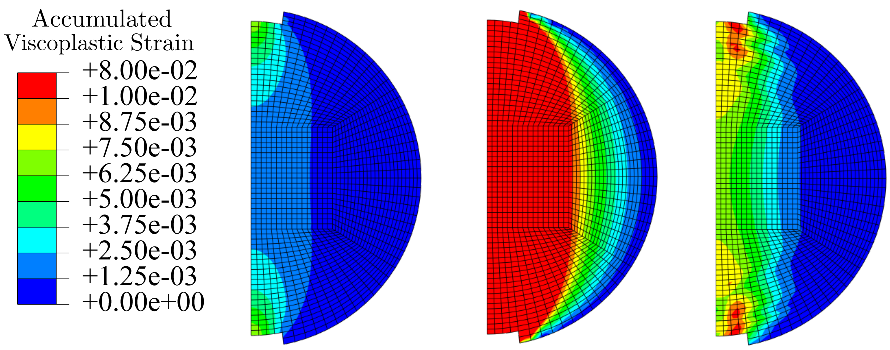

(a) (b) (c)

Figure 12: Accumulated viscoplastic strain distribution on a Brazilian test sample. (a) compression (b) tension and (c) asymmetric material properties.

experiments needs to be done. Figure 13 shows the variation of the vertical displacement u_y of the top of the sample as a function of time, according to the change of the parameters.

Table 2: Variation of the material parameters − Isotropic creep model

Parameter	+10%	+20%	−10%	−20%
$\log_{10} A^{-} [\text{MPa}^{-n} s^{-1}]$	−15.57	−16.99	−12.74	−11.32
$n^{-}[-]$	4.35	4.75	3.56	3.16
$m^{-}[-]$	−3.01	−3.28	−2.46	−2.19
$\log_{10} A^{+} [\text{MPa}^{-n} s^{-1}]$	−5.94	−6.48	−4.86	−4.32
$n^{+}[-]$	1.65	1.8	1.35	1.2

Figures 13a, 13b and 13c show the influence of the compression parameters A^{-}, n^{-} and m^{-}, respectively. The curve with the variation of -20% was not plotted, since the displacement was excessively high, due to the large influence of this parameter in the results. It is possible to observe that parameter n^{-}, that is an exponent of the stress, has a negligible influence on the results, due to the low values of stresses in this application. Parameters A^- and m^- influence mostly the beginning of the curve, changing its curvature radius, indicating that the compression stresses are predominant during the first hour, and the tensile stresses take over from this point further. This is an important conclusion, since it helps to decide in which part of the curve the identification procedure will focus, depending on the desired result.

Similarly, A^+ has the higher influence among the tensile parameters, as can be observed in Figures 13d and 13e, although n^+ starts to be influent after one hour of loading and can become more meaningful for longer periods. Contrary to the compressive parameters, the tensile parameters, specially A^+, change mainly the slope of the curve after the initial curvature has passed. Again, this remarkable separation in time between the influence of the tensile and compressive parameters facilitates the inverse identifications.

5. Experimental methodology

In this work, Brazilian tests were used to identify the creep parameters of an alumina-spinel material. Traditionally, Brazilian tests have been applied to study the tensile strength of concretes and geomaterials, as a replacement to direct tensile tests. As pointed by several studies, the results of a Brazilian test to calculate the tensile strength of a given material is only valid if the crack initiation is at the center of the sample, and not at the stress concentrations present at the contact points (Darvell, 1990; Fairhurst, 1964; García et al., 2017). For the applications in the current work, the position of the initiation of the crack is not important, since no fracture is expected during the test.

The Brazilian test was chosen for the identification of the asymmetric creep parameters due to the complexity of the stress field developed in the sample during the application of the load. As shown in Figure 14, tensile stresses are developed at the center of the sample, while compressive stresses start to increase towards its borders and shear stresses are present in the regions in contact with the upper and lower jaws. A more detailed description of the

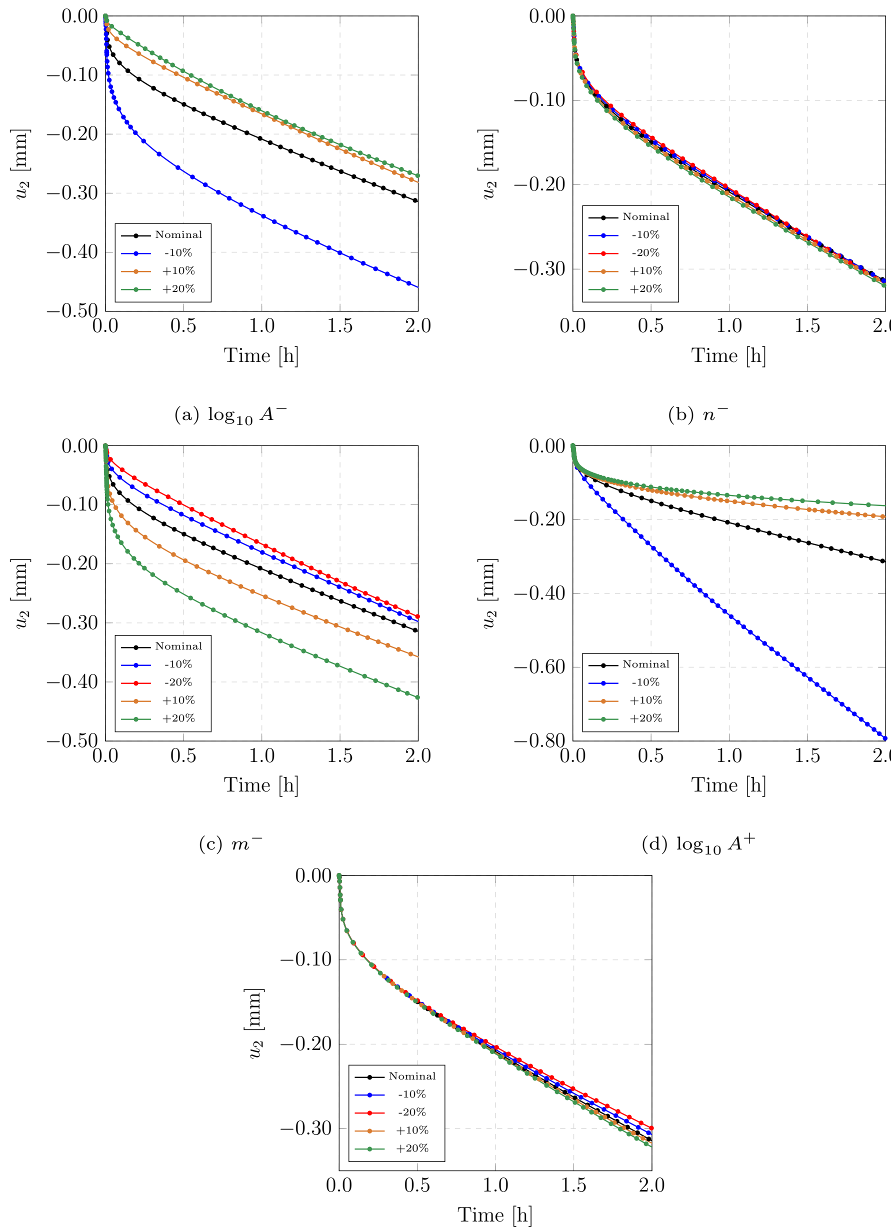

(a) $\log_{10} A^-$

(b) n^-

(c) m^-

(d) $\log_{10} A^+$

(e) n^+

Figure 13: Change on the asymmetric creep model response due to variations of the material parameters − Brazilian test.

stress equations related to the Brazilian test can be found in Fahad (1996). This stress distribution is adapted to the current case, since it allows the study of the effect of the material properties under tension and compression using a single test, which considerably reduces the number of experiments that need to be performed.

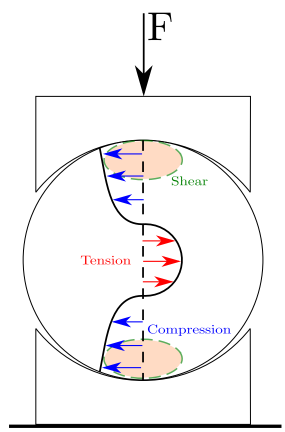

Figure 14: Stress distribution in a Brazilian test sample

The application of Brazilian tests to refractory materials is still limited, specially regarding the characterization of creep behavior. Belrhiti et al. (2017) used this test in association to a DIC technique to characterize the mechanical behavior of magnesia hercynite refractories used in cement rotary kilns, estimating the elastic modulus, Poisson's ratio and fracture energy at room temperature. Gazeau et al. (2015) used the Brazilian test associated with the integrated DIC technique to identify the Young's modulus and the tensile strength of plane membranes at temperatures up to 900 °C. These two applications demonstrate the potential of this method to provide various information using a single experimental setup, what can result in the reduction of the required number of tests to characterize a material. This is specially important considering the cost and time demand of high temperature tests.

5.1. *Experimental setup*

In this work, the Brazilian test was used in association with a DIC technique. This technique is convenient for the current application, since the traditional instrumentation of testing setups at high temperatures present significant difficulties.

Previous works have given detailed information about DIC applications at high temperatures (Leplay et al., 2015; Leplay et al., 2010, 2012; Novak & Zok, 2011). When pictures at high temperatures need to be taken, the excessive black body radiation coming from the furnace needs to be filtered, otherwise the image is oversaturated and presents no contrast. This is frequently achieved by using blue band pass filters, and sometimes neutral density filters depending on the exposure time of the pictures, that only allows that the blue part of the light spectrum arrives at the camera sensors. To increase the quality of the pictures, it is also common to enlighten the sample using a blue light source.

Figure 15 shows the experimental setup used to perform the Brazilian tests and to take the pictures at high temperatures. This setup is composed of the following parts:

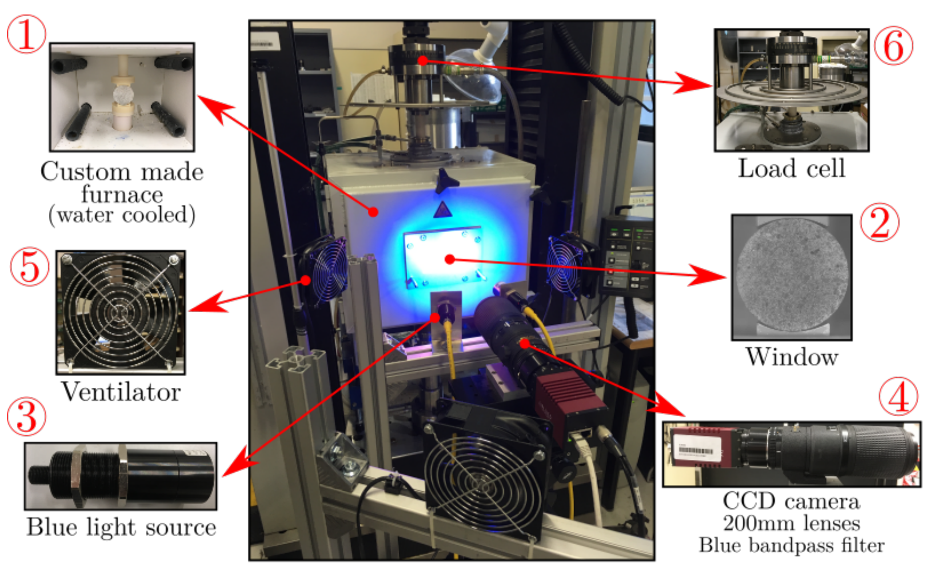

Figure 15: Experimental setup for the Brazilian tests at high temperature

1. A water cooled custom made furnace with the capacity to heat up to 1300 °C.
2. The furnace's door is equipped with a window made of a vitro ceramic material, so that the sample can be photographed. This material was chosen because of its adequate resistance to temperatures up to 1300 °C, its low thermal expansion and its inexpensive price. The material is transparent enough to allow that satisfactory pictures are taken.
3. To increase the amount of blue light available when taking the pictures, two blue light sources are used to enlighten the sample. In combination with the blue filters, this increases significantly the contrast of the pictures, to a point where the DIC analysis becomes possible. These lights are mounted in a dedicated support that was designed to offers six degrees of freedom, so they can be easily positioned to avoid glare in the pictures.
4. A high resolution 12 bit CCD camera, AF Micro-Nikkor 200 mm lenses and a blue band pass filter, to decrease the amount of light being captured by the camera, since it blocks all parts of the optical spectrum that are not blue, avoiding the saturation of the sensor.
5. The camera and the lenses are cooled using two ventilators, since they stand close to the furnace and can overheat. A third ventilator is used to blow away the hot air between the window and the lenses, minimizing the generation of heat hazes.
6. A load cell with maximum capacity of 30 kN.

The samples used in the Brazilian tests were cut from parallel refractory bricks. The first step was to cut slices 40 mm thick, to guarantee the parallelism of the sample surface exposed to the camera. Second, 50 mm cylinders were drilled from these slices. This geometry was chosen to comply with a rule of thumb on the refractories field that requires the minimum dimension of the sample to be at least 10 times the size of the largest grain in the material, that, in the case of the alumina-spinel brick, is 3 mm.

To improve the contrast of the samples surfaces, a SiC powder speckle pattern was used, with grain sizes varying from 50 μm to 100 μm. The surfaces of the sample were covered with a bonding agent, and the powder was deposited using a sieve, similar to what was done by Archer et al. (2020), what allowed a reasonable control over the particles dispersion. Using this method, the speckle does not remain strongly attached to the sample, and, even if it does not detach under simple gravitational action, direct contact with it should be avoided. Before the test, the sample was let at rest for 12 hours, in order to dry the excess of the bonding agent. Figure 17a shows an example of a sample coated with a speckle pattern, already positioned at the testing machine.

To guarantee the good quality of the pictures, a rigorous procedure was followed at each test. This procedure was composed of:

1. The sample and the jaws were positioned at the testing machine at room temperature, and an initial pre-load of approximately 50 N was applied.
2. The furnace was closed, and the heating of the sample started. Figure 16 shows the heating curves used for the tests. Between room temperature and 600 °C, a heating rate of 10 °C/min was used. From 600 °C to 1300 °C, this rate was reduced to 5 °C, to avoid thermal damage on the sample and on the equipment. Before the beginning of the test, the furnace was let in a dwell for 1 h, to stabilize the temperature of the testing setup. The blue curve on Figure 16, obtained from one of the tests made at 1300 °C, shows that the displacement of the machine piston was constant before the end of the dwell, indicating that there was no extra thermal expansion of the equipment at the beginning of the test.
3. After the temperature homogenization time was passed, the camera lenses and the blue band pass filter were cleaned to remove any dust particles that could cause artifacts in the pictures and later mounted on the camera. To increase the images contrast, the blue lights were positioned to generate the maximum illumination of the sample as possible, avoiding glare, and the focus was manually adjusted in order to increase the sharpness. The exposure time was adjusted according to the lightning conditions to avoid

too bright or too dark images.

4. The sample was loaded at a rate of 0.5 mm/min until the creep load was achieved, and the force was held constant until the end of the test.

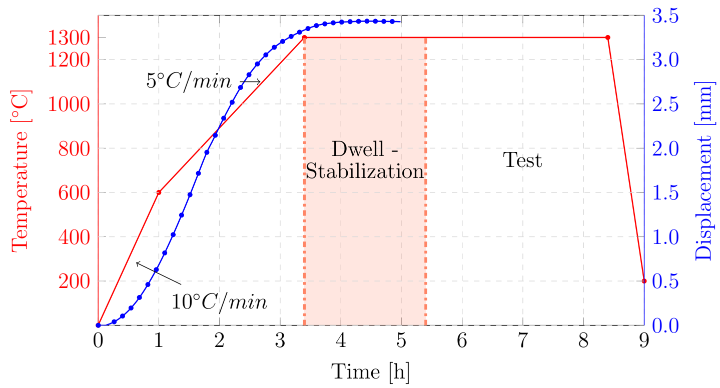

Figure 16: Heating curve and evolution of machine displacements prior to the test.

Figure 17 shows the effect of the lightning and of the blue band pass filter in the quality of the images. At room temperature (Figure 17a), the histogram of the image, shown in Figure 18, is approximately normally distributed around gray values from 75 to 200, and the image presents a high contrast. At 1200 °C, without the use of the blue lights and of the blue band pass filter (Figure 17b), the distribution of gray levels is restricted to the range between 105 and 115, and the images looses most of its contrast. The use only of the blue band pass filter, without the blue lights (Figure 17c), slightly decreases the sharpness of the histogram, but not enough to guarantee enough contrast. Finally, using the blue lights and filter (Figure 17d), the gray level distribution becomes closer to that of the image at room temperature, and most of the contrast is recovered.

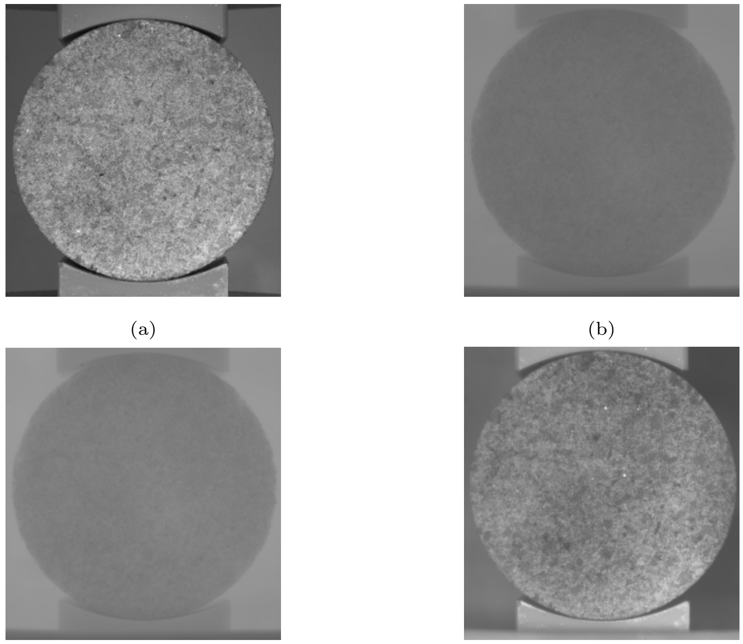

(a) (b) (c) (d)

Figure 17: Influence of the blue light and the blue band pass filter in the quality of the image. (a) Image at room temperature. (b) No blue light and no filter. (c) No filter. (d) Use of blue light and blue band pass filter.

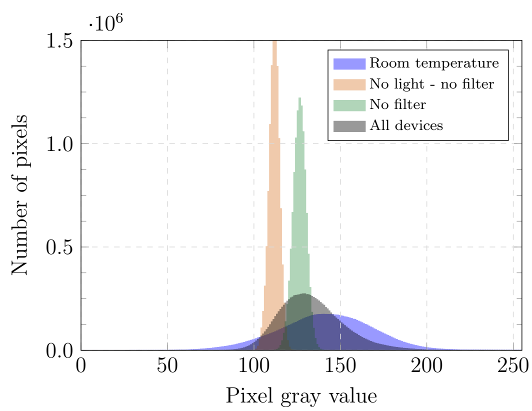

Figure 18: Histograms of the images at room and high temperature.

The open-source DIC software Ncorr (Blaber et al., 2015) was used to calculate the full field displacements of the samples. Ncorr uses the local subset-based reliability-guided DIC method according to Pan (2009).

6. Identification of the asymmetric creep properties for the alumina-spinel material at 1300 °C

Figure 19 shows the relative vertical displacement of the upper point of the Brazilian test samples at 1300 °C, calculated using DIC, that corresponds to the difference between the vertical displacements at the upper part and the vertical displacements at the lower part, to account for rigid body movements of the experimental setup. It is possible to observe that samples 1, 3, 5 and 6 are in good agreement, while samples 2 and 4 are lower and upper outliers, respectively.

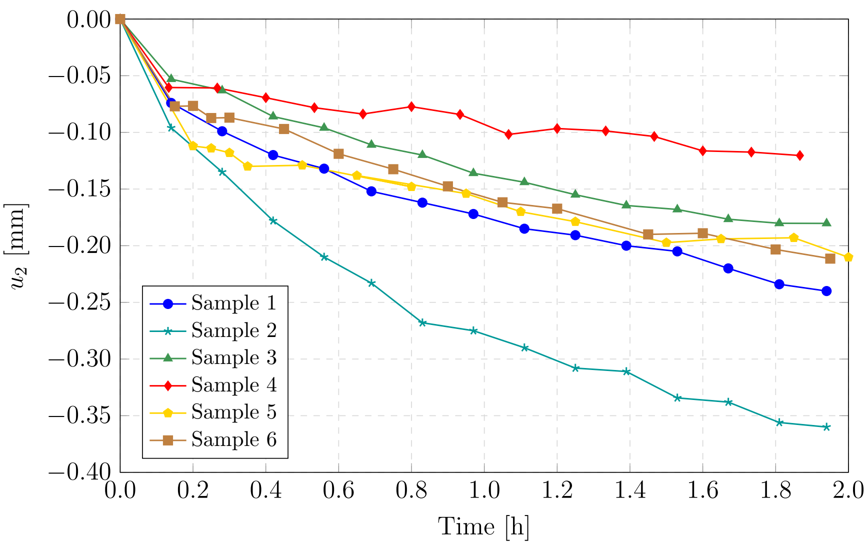

Figure 19: Brazilian tests time vs displacement curves obtained by DIC.

Figure 20 shows an example of envelope for the material parameters at 1300 °C, obtained through a series of numerical simulations using the asymmetric creep model presented in Section 3. It can be expected that the material parameters will not highly deviate from the ones presented in the figure, even if this analysis only considers a single displacement value, and not the full field.

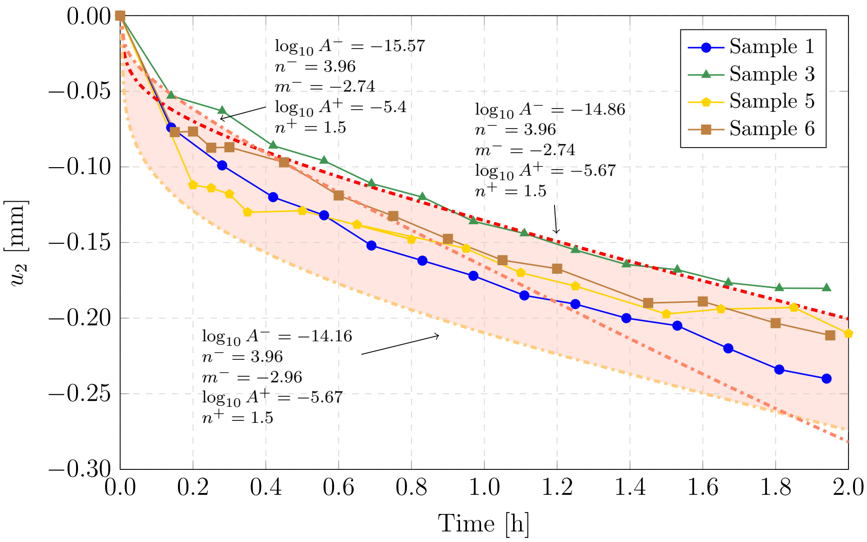

Figure 20: Brazilian tests time vs displacement curves and parameters envelope.

Finally, taking into account the influence of the material parameters in each portion of the time vs displacement curve for Brazilian tests presented in Section 4.2.1, the parameters for the alumina-spinel material were identified in order to better approximate the values of the DIC calculations, and the resulting curve is presented in Figure 21. The identified parameters are shown in Table 3.

Table 3: Identified material parameters

Parameter	**Compression**	**Tension**
$\log_{10} A[\text{MPa}^{-n} s^{-1}]$	−14.86	−5.55
$n[-]$	3.96	1.5
$m[-]$	−2.74	–

From Figure 21 it is possible to observe that the identified curve fits the experimental values with good accuracy. The full DIC displacement field of sample 6 was compared with the results of numerical simulations performed using the identified material parameters, to verify the robustness of the identification.

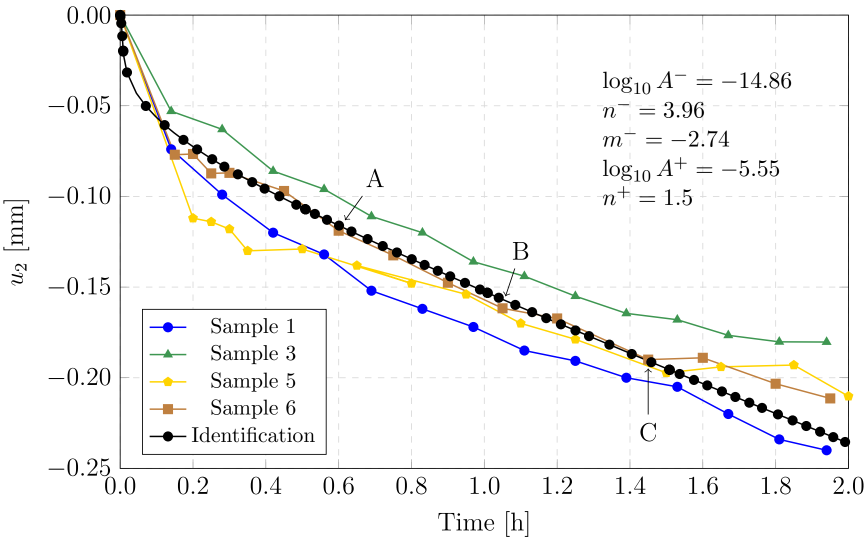

Figure 21: Brazilian tests time vs displacement curves and inverse identification.

The vertical displacements fields of Points A, B and C represented in Figure 21, corresponding to $t = 0.6$ h, $t = 1.05$ h and $t = 1.45$ h, respectively, are shown in Figure 22. It is possible to see that there is a rigid body rotation of the sample, since the displacements map does not correspond to the traditional displacements field of Brazilian tests. To consider this effect, an extra identification calculation was made to determine what is the magnitude of the load that caused this deviation. An horizontal load of -7 N was identified and applied on the upper jaws in the simulation model. This corresponds to an error of 0.5° in the application of the load, which shows that the experimental procedure is sensitive to small deviations from the ideal boundary conditions.

Figure 23 shows the results of the numerical simulations using the previously identified material parameters and the horizontal load. It is possible to observe that the displacement maps of Figures 22 and 23 have a good equivalence, despite the experimental errors and the simplicity of the identification procedure.

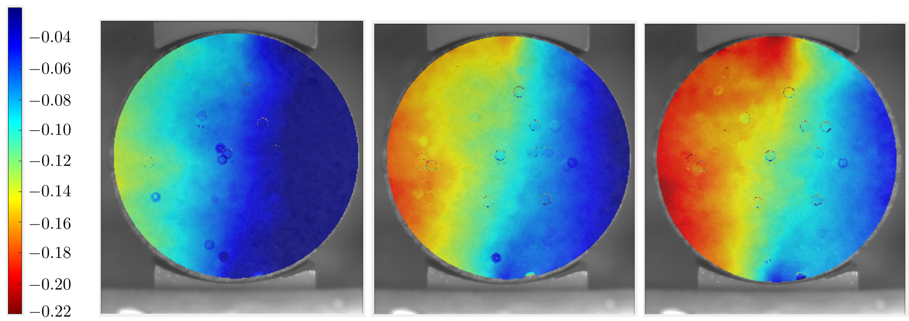

(a) (b) (c)

Figure 22: Brazilian tests: Vertical displacement in mm at 1300 °C − DIC sample 6. (a) Point A. (b) Point B. (c) Point C.

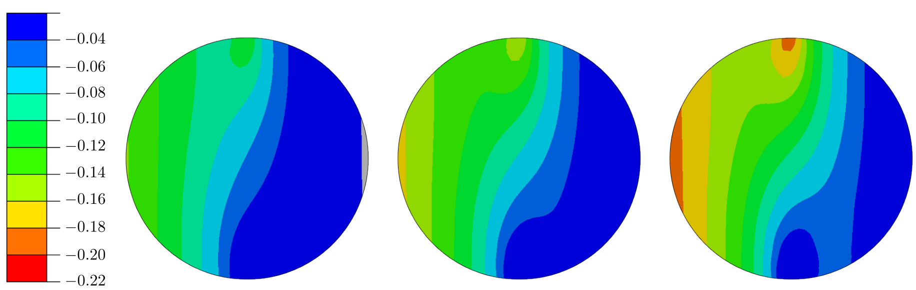

(a) (b) (c)

Figure 23: Brazilian tests: Vertical displacement in mm at 1300 °C − Simulation. (a) Point A. (b) Point B. (c) Point C.

It is interesting to observe how the vertical displacement of the central line of the sample changes when the rigid body motions are included in the simulation, as shown in Figure 24. When the boundary conditions are symmetric, the displacement increases monotonically and equally in both sides of the sample, as expected. Nevertheless, a horizontal force in the negative x direction causes an increase in the magnitude of the displacements at the right side of the sample (point A in Figure 24), while the left side presents a positive displacement during loading (point B in Figure 24). After approximately 1 h of creep defor-

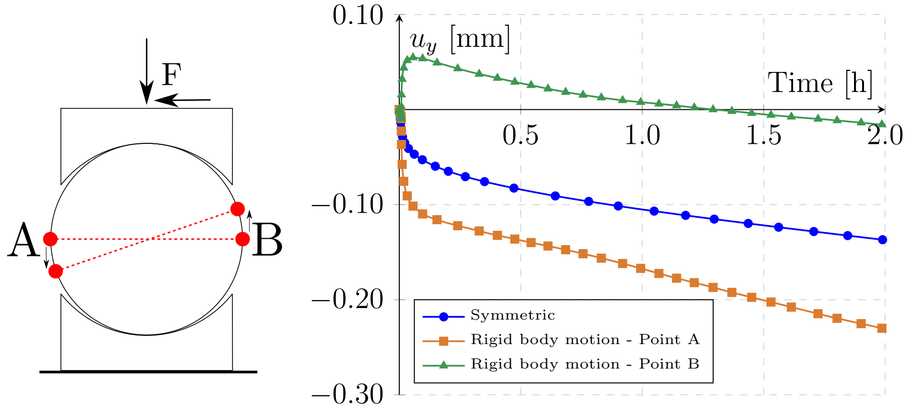

Figure 24: Brazilian tests: Vertical displacement of points A and B.

mations, the displacement of the right side becomes negative again, but always smaller than at the left. This non-symmetric behavior, caused by imperfections in the boundary and loading conditions, is frequently observed in mechanical experiments (de Melo et al., 2020) and has the potential to negatively influence the DIC identifications if not properly considered.

7. Conclusions

From previous publications available in the literature, it is clear that refractory materials present a different creep behavior under tension and compression. Therefore, there is a need to develop a dedicated model, considering that this feature is not currently available in the main commercial Finite Element Analysis software. In the present work, an asymmetric creep model was proposed, that was especially designed to simulate refractory materials at high temperatures. In comparison to previously published works, the proposed model has the advantage to be able to represent the primary and secondary creep behavior of the material, while keeping the possibility to have independent tests for the identification of tension and compression parameters.

The main strategy employed in the development of the model was the split of the stress tensor into a positive and a negative part, similar to what have been done by Blond et al. (2005), but averaging the contributions of each stress sign by the equivalent stresses. In this case, the model tends to its symmetric version when the same material properties are used for both signs.

To identify the material parameters of an alumina-spinel material at 1300 °C, an experimental procedure composed of a Brazilian test in combination with a subset-based DIC technique was developed, that avoids the problems related to contact instrumentation at high temperatures. This technique showed to be successful for the determination of the model parameters.

Acknowledgments

This work was supported by the funding scheme of the European Commission, Marie Skłodowska-Curie Actions Innovative Training Networks in the frame of the project ATHOR - Advanced THermomechanical multiscale mOdelling of Refractory linings 764987 Grant. The authors acknowledge the company RHI Magnesita for providing the alumina-spinel material.

References

Altenbach, H. (2001). Consideration of Stress State Influences in the Material Modelling of Creep and Damage. In S. Murakami & N. Ohno (Eds.), *IUTAM Symposium on Creep in Structures* (pp. 141–150). Springer Netherlands. https://doi.org/10.1007/978-94-015-9628-2_15

Archer, T., Beauchêne, P., Huchette, C., & Hild, F. (2020). Global digital image correlation up to very high temperatures with grey level corrections. *Measurement Science and Technology*, *31*(2), 024003. https://doi.org/10.1088/1361-6501/ab461e

Banerjee, S. (2004). Properties of Refractories. *Refractories Handbook* (First, pp. 1–10). Marcel Dekker, Inc.

Belrhiti, Y., Dupre, J., Pop, O., Germaneau, A., Doumalin, P., Huger, M., & Chotard, T. (2017). Combination of Brazilian test and digital image correlation for mechanical characterization of refractory materials. *Journal of the European Ceramic Society*, *37*(5), 2285–2293. https://doi.org/10.1016/j.jeurceramsoc.2016.12.032

Benallal, A., Billardon, R., & Doghri, I. (1988). An integration algorithm and the corresponding consistent tangent operator for fully coupled elastoplastic and damage equations. *Communications in Applied Numerical Methods*, *4*(6), 731–740. https://doi.org/10.1002/cnm.1630040606

Blaber, J., Adair, B., & Antoniou, A. (2015). Ncorr: Open-Source 2D Digital Image Correlation Matlab Software. *Experimental Mechanics*, *55*(6), 1105–1122. https://doi.org/10.1007/s11340-015-0009-1

Blond, E., Schmitt, N., Hild, F., Blumenfeld, P., & Poirier, J. (2005). Modelling of high temperature asymmetric creep behavior of ceramics. *Journal of the European Ceramic Society*, *25*(11), 1819–1827. https://doi.org/10.1016/j.jeurceramsoc.2004.06.004

Darvell, B. W. (1990). Uniaxial compression tests and the validity of indirect tensile strength. *Journal of Materials Science*, *25*(2), 757–780. https://doi.org/10.1007/BF03372161

de Melo, C. C., Furlan, M., Hild, F., Schmitt, N., & Canto, R. B. (2020). Uniaxial compression test on ceramic green compact with bending consideration using digital image correlation. *Powder Technology*, *376*, 136–148. https://doi.org/10.1016/j.powtec.2020.08.002

Dutta, S. K., & Chokshi, Y. B. (2020). *Basic Concepts of Iron and Steel Making*. Springer Singapore. https://doi.org/10.1007/978-981-15-2437-0

Esposito, L., & Bonora, N. (2011). A primary creep model for Class M materials. *Materials Science and Engineering: A*, *528*(16-17), 5496–5501. https://doi.org/10.1016/j.msea.2011.03.069

Fahad, M. K. (1996). Stresses and failure in the diametral compression test. *Journal of Materials Science*, *31*(14), 3723–3729. https://doi.org/10.1007/BF00352786

Fairhurst, C. (1964). On the validity of the 'Brazilian' test for brittle materials. *International Journal of Rock Mechanics and Mining Sciences & Geomechanics Abstracts*, *1*(4), 535–546. https://doi.org/10.1016/0148-9062(64)90060-9

García, V. J., Márquez, C. O., Zúñiga-Suárez, A. R., Zuñiga-Torres, B. C., & Villalta-Granda, L. J. (2017). Brazilian Test of Concrete Specimens Subjected to Different Loading Geometries: Review and New Insights. *International Journal of Concrete Structures and Materials*, *11*(2), 343–363. https://doi.org/10.1007/s40069-017-0194-7

Gazeau, C., Gillibert, J., Blond, E., Geffroy, P.-M., & Richet, N. (2015). Experimental set up for the mechanical characterization of plane ITM membrane at high temperature. *Journal of the European Ceramic Society*, *35*(14), 3853–3861. https://doi.org/10.1016/j.jeurceramsoc.2015.06.026

Jin, S., Harmuth, H., & Gruber, D. (2014). Compressive creep testing of refractories at elevated loads - Device, material law and evaluation techniques. *Journal of the European Ceramic Society*, *34*(15), 4037–4042. https://doi.org/10.1016/j.jeurceramsoc.2014.05.034

Jin, S., Harmuth, H., Gruber, D., & Rössler, R. (2015). Influence Of Creep On The Thermomechanical Behavior Of a RH-Snorkel. *Unified International Technical Conference on Refractories*, 4.

Jin, S., Harmuth, H., Gruber, D., Buhr, A., Sinnema, S., & Rebouillat, L. (2020). Thermomechanical modelling of a torpedo car by considering working lining spalling. *Ironmaking & Steelmaking*, *47*(2), 145–149. https://doi.org/10.1080/03019233.2018.1495797

Jin, S., Harmuth, H., Gruber, D., & Li, Y. (2011). Classification of Thermomechanical Impact Factors and Prediction Model for Ladle Preheating. *J Wuhan Univ Sci Technol*, *34*, 8.

Lemaître, J., & Chaboche, J. (1990). *Mechanics of solid materials*. Cambridge University Press.

Leplay, P., Lafforgue, O., & Hild, F. (2015). Analysis of Asymmetrical Creep of a Ceramic at 1350°C by Digital Image Correlation. *Journal of the

American Ceramic Society, *98*(7), 2240–2247. https://doi.org/10.1111/jace.13601

Leplay, P., Réthoré, J., Meille, S., & Baietto, M.-C. (2010). Damage law identification of a quasi brittle ceramic from a bending test using Digital Image Correlation. *Journal of the European Ceramic Society*, *30*(13), 2715–2725. https://doi.org/10.1016/j.jeurceramsoc.2010.05.021

Leplay, P., Réthoré, J., Meille, S., & Baietto, M.-C. (2012). Identification of asymmetric constitutive laws at high temperature based on Digital Image Correlation. *Journal of the European Ceramic Society*, *32*(15), 3949–3958. https://doi.org/10.1016/j.jeurceramsoc.2012.03.024

Mahnken, R. (2003). Creep simulation of asymmetric effects by use of stress mode dependent weighting functions. *International Journal of Solids and Structures*, *40*(22), 6189–6209. https://doi.org/10.1016/S0020-7683(03)00388-3

Naumenko, K., & Altenbach, H. (2007). *Modeling of Creep for Structural Analysis* (V. I. Babitsky & J. Wittenburg, Eds.). Springer Berlin Heidelberg. https://doi.org/10.1007/978-3-540-70839-1

Novak, M. D., & Zok, F. W. (2011). High-temperature materials testing with full-field strain measurement: Experimental design and practice. *Review of Scientific Instruments*, *82*(11), 115101. https://doi.org/10.1063/1.3657835

Pan, B. (2009). Reliability-guided digital image correlation for image deformation measurement. *Applied Optics*, *48*(8), 1535. https://doi.org/10.1364/AO.48.001535

Samadi, S., Jin, S., Gruber, D., Harmuth, H., & Schachner, S. (2020). Statistical study of compressive creep parameters of an alumina spinel refractory. *Ceramics International*, *46*(10, Part A), 14662–14668. https://doi.org/10.1016/j.ceramint.2020.02.267

Samadi, S., Jin, S., & Harmuth, H. (2021). Combined damaged elasticity and creep modeling of ceramics with wedge splitting tests. *Ceramics Inter-*

national, *47*(18), 25846–25853. https://doi.org/10.1016/j.ceramint.2021.05.315

Schachner, S., Jin, S., Gruber, D., & Harmuth, H. (2019). Three stage creep behavior of MgO containing ordinary refractories in tension and compression. *Ceramics International*, *45*(7), 9483–9490. https://doi.org/10.1016/j.ceramint.2018.09.124

Schacht, C. A. (2004). Thermomechanical Considerations for Refractory Linings. *Refractories Handbook* (First, pp. 369–394). Marcel Dekker, Inc.

Sidi Mammar, A., Gruber, D., Harmuth, H., & Jin, S. (2016). Tensile creep measurements of ordinary ceramic refractories at service related loads including setup, creep law, testing and evaluation procedures. *Ceramics International*, *42*(6), 6791–6799. https://doi.org/10.1016/j.ceramint.2016.01.056

Teixeira, L., Samadi, S., Gillibert, J., Jin, S., Sayet, T., Gruber, D., & Blond, E. (2020). Experimental Investigation of the Tension and Compression Creep Behavior of Alumina-Spinel Refractories at High Temperatures. *Ceramics*, *3*(3), 372–383. https://doi.org/10.3390/ceramics3030033

Volkova, O., & Janke, D. (2005). Influence of the Lining on the Thermal Behaviour of a Teeming Ladle. *steel research international*, *76*(4), 313–319. https://doi.org/10.1002/srin.200506014
_eprint: https://onlinelibrary.wiley.com/doi/pdf/10.1002/srin.200506014